Research Article

Christoph Holst*, Axel Nothnagel, Martin Blome, Philip Becker, Malwin Eichborn, and Heiner Kuhlmann

Improved area-based deformation analysis of a radio telescope's main reflector based on terrestrial laser scanning

Abstract: The main reflectors of radio telescopes deform due to gravitation when changing their elevation angle. This can be analyzed by scanning the paraboloid surface with a terrestrial laser scanner and by determining focal length variations and local deformations from best-fit approximations.

For the Effelsberg radio telescope, both groups of deformations are estimated from seven points clouds measured at different elevation angles of the telescope: the focal length decreases by 22.7 mm when tilting the telescope from 90 deg to 7.5 deg elevation angle. Variable deformations of ± 2 mm are detected as well at certain areas. Furthermore, a few surface panels seem to be misaligned.

Apart from these results, the present study highlights the need for an appropriate measurement concept and for preprocessing steps when using laser scanners for area-based deformation analyses. Especially, data reduction, object segmentation and laser scanner calibration are discussed in more detail. An omission of these steps would significantly degrade the deformation analysis and the significance of its results. This holds for all sorts of laser scanner based analyses.

Keywords: terrestrial laser scanner, area-based deformation analysis, object segmentation, data reduction, self-calibration

DOI 10.1515/jag-2014-0018
Received August 14, 2014; accepted October 23, 2014.

***Corresponding Author: Christoph Holst:** Institute of Geodesy and Geoinformation, University of Bonn, Germany, E-mail: c.holst@igg.uni-bonn.de
Axel Nothnagel, Martin Blome, Philip Becker, Malwin Eichborn, Heiner Kuhlmann: Institute of Geodesy and Geoinformation, University of Bonn, Germany

1 Motivation

Radio telescopes are often used for geodetic very long baseline inteferometry (VLBI) measurements. By simultaneously measuring the differences in signal arrival times, the vectors between the reference points of pairs of radio telescopes can be estimated. The signal paths within the optics of the radio telescopes do not influence the observation if they remain constant because they are absorbed in the clock corrections [1, 34].

This is not the case if the focal length of a telescope's main reflector underlies variations since this also results in a variation of the signal path [4]. Hence, focal length variations can affect the VLBI observable to a non-negligible extent. Figure 1 displaying the Effelsberg radio telescope exemplarily shows two distinct signal paths explaining this situation. Since these signals are reflected on the main reflector (afterwards reflected on the subreflector and finally bundled in the feed horn), local variations in its shape also lead to signal variations biasing the VLBI observable. Consequently, both the focal length of a radio telescope and its main reflector's shape, should be known very accurately.

Determining the focal length and the main reflector's detailed shape is not trivial since both parameters vary due to gravitation when changing the telescope's elevation angle. This has already been analyzed for several radio telescopes [11, 15, 35, 36, 40, 41]. Here, either photogrammetric or terrestrial laser scanner (TLS) measurements have been used for analysis – each time by high density sampling of the main reflector's surface.

Comparing both approaches, the ability of using photogrammetric measurements is limited to small reflectors only, e.g., reflectors of 12 m [40] or 22 m [41] in diameter have been measured. This is due to the number of photographs that need to be taken for a detailed capturing of the reflector's shape as well as due to the subsequent bundle adjustment that needs a large number of targets to be mounted on the complete reflector's surface [40, 41]. Ter-

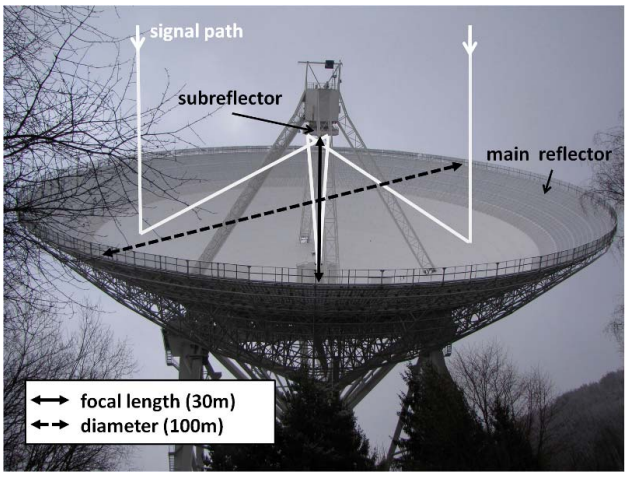

Fig. 1. Effelsberg radio radio telescope with a sketch of two distinct single paths [15].

restrial laser scans do not suffer from these limitations; they are used for scanning reflectors of 30 m [5], 32 m [35] and of even 100 m [15] in diameter.

The 100 m Effelsberg radio telescope – being investigated in the present study – has already been scanned for deformation analysis in the year 2010. Based on these scans, changes in the shape of the main reflector leading to focal length variations of several millimeters have been revealed using the Leica HDS 6100 laser scanner [11, 14, 15, 31]. However, the measurement concept and the data processing needed to be further improved. This is a consequence of the progress in knowledge regarding the measurement and processing of laser scanner point clouds that took place in recent years. This especially holds for data reduction of point clouds [10, 14] and the calibration of TLS [13]. Additionally, new measurements of the Effelsberg radio telescope have been performed in the year 2013 using the laser scanner Leica Scan Station P20.

Thus, the improved deformation analysis of the Effelsberg radio telescope presented here can be regarded as a result of steady enhancement of using laser scanner measurements for surface analysis. At the end, focal length variations and local deformations can be revealed with a precision in the range of a millimeter. This is possible since the shape of the scanned object – a rotational paraboloid – is known. Hence, the crucial step for a precise analysis is the integration of model knowledge.

In the following sections, the different steps of deformation analysis are presented. Especially, the improved measurement concept, the data reduction, the object segmentation and the TLS calibration need to be applied since all of these steps essentially upgrade the significance of the derived results. In the corresponding sections, the improved analysis is described and compared to the processing steps commonly applied up to now. Finally, the global deformation (focal length variations) as well as the local deformations (systematic deviations from the best-fit surface) of the Effelsberg radio telescope are presented and discussed.

2 Measurement concept

The Effelsberg radio telescope's diameter is 100 m, its focal length approx. 30 m and its weight 3200000 kg [28]. The scanning concept for this telescope, developed already in 2010 [15], is based on the requirement that the complete main reflector can be covered from a single scanner position.

For this purpose, the scanner is mounted head-down near the prime focus underneath the Gregorian subreflector. With this setup, only the areas shaded by the beams holding the subreflector cannot be covered. In the first measurement project in 2010, the TLS had been fixed rigidly to the structure so that it rotated entirely with the main reflector [15]. As a consequence, the bearings and the servomotors rotating the TLS in azimuth and those actuating the beam deflection had been subject to forces which may lead to damages of the TLS or to biased measurements. Thus, this measurement concept needed to be upgraded.

As a consequence of these drawbacks, the new design forsees that the TLS always stays in a vertical position, although upside-down again, even at different elevation angles of the telescope. For this purpose, a stable hinge was constructed (Figure 2) which allows the TLS to respond to tilting like a pendulum. The hinge is equipped with a strong brake which is released when the elevation angles of the telescope are changing and fixed when measuring. Consequently, the complete radio telescope as well as the TLS mount can be assumed to remain fixed during each scan.

Using this hinge in the same position as in the previous project (underneath the Gregorian subreflector), the main reflector was scanned with a Leica Scan Station P20 in seven different elevation angles of 90 deg, 75 deg, 60 deg, 45 deg, 30 deg, 15 deg and 7.5 deg covering the normal range of operation. Each scan produced a point cloud consisting of approx. 500 million points with measured distances from 30 m to 50 m. These measurements were performed at night to avoid solar radiation degrading the scans.

Fig. 2. Station and orientation of the TLS at an elevation angle of the telescope of 90 *deg* (left) and 7.5 *deg* (right).

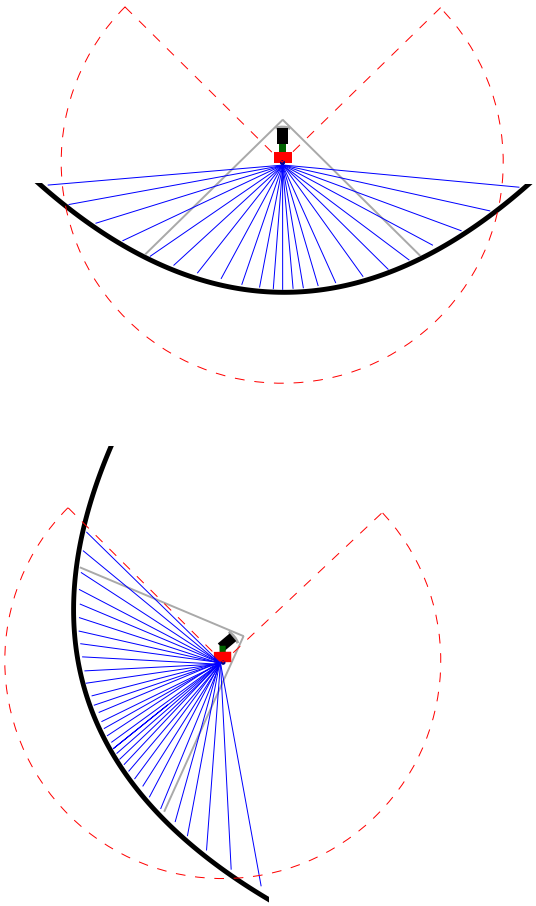

Fig. 3. Sketch of the measurement geometry, the resulting laser beam vectors (blue) inside the laser scanners's field-of-view (red dashed) and the elevation of the telescope's main reflector (black); 90 *deg* elevation (top) and 30 *deg* elevation (bottom)

During these measurements, the dual-axis compensator of the TLS was always switched off. The TLS does not have to be levelled (upside-down) for this project since only the shape of the main reflector is analyzed, not its absolute spatial transformation. Small deviations from this upside-down position – that is only required by the TLS servomotors – are, thus, irrelevant.

A disadvantage of the upgraded measurement geometry is that the main reflector cannot be scanned completely at low elevation angles due to the limited vertical field-of-view of 270 *deg* of the TLS. This is depicted in Figure 3 where a small part at the top of the main reflector is outside of the field-of-view of the TLS.

3 Parameter estimation

The seven measured point clouds each consisting of $j = 1, \ldots n$ sampling points are parameterized by the functional model of the main reflector equaling a rotational paraboloid [9]. A rotational paraboloid can be represented only by one parameter describing its form, i.e., the focal length f, if it is positioned in its normal form where its rotation axis equals the Z-axis of the coordinate system $[X, Y, Z]$:

$$\frac{X_j^2 + Y_j^2}{4 \cdot f} - Z_j = 0. \tag{1}$$

This is not the case when the main reflector is scanned in the laser scanner's local coordinate system $[x, y, z]$, so that the paraboloid needs to be transformed by

$$\mathbf{X}_j = \begin{bmatrix} X_j \\ Y_j \\ Z_j \end{bmatrix} = \mathbf{R}_y(\varphi_y) \cdot \mathbf{R}_x(\varphi_x) \cdot \mathbf{x}_j + \mathbf{X}_v \tag{2}$$

where $\mathbf{R}_x$ and $\mathbf{R}_y$ are the rotation matrices around the x- and y- axis and $\mathbf{X}_v$ the translation vector. Consequently, the parameters describing the rotational paraboloid inside the laser scanner's coordinate system are

$$\mathbf{p} = [X_v, Y_v, Z_v, \varphi_x, \varphi_y, f]^T. \tag{3}$$

These have to be estimated based on the sampling coordinates $\mathbf{x}_j$. These are themselves a result of the original polar measurements with

$$\mathbf{x}_j = \begin{bmatrix} x_j \\ y_j \\ z_j \end{bmatrix} = \begin{bmatrix} s_j \cdot \sin\beta_j \cdot \cos t_j \\ s_j \cdot \sin\beta_j \cdot \sin t_j \\ s_j \cdot \cos\beta_j \end{bmatrix} \tag{4}$$

where $\mathbf{l}_j = [s_j, \beta_j, t_j]$ and with s being the distance, β the vertical angle and t the horizontal direction.

Consequently, for estimating the parameters $\mathbf{p}$ (eq. 3), the original polar measurements of the TLS $\mathbf{l}_j$ are integrated in the paraboloid's model (eq. 1) by transformation into cartesian coordinates $\mathbf{x}_j$ (eq. 4) and then by transformation into the coordinates $\mathbf{X}_j$ of the paraboloid's coordinate system (eq. 2). All three steps together build up the functional model of the adjustment for estimating the parameters.

For the stochastic model, the covariance matrix

$$\boldsymbol{\Sigma}_{ll,j} = \begin{bmatrix} \sigma_{s,j}^2 & & \\ & \sigma_\beta^2 & \\ & & \sigma_t^2 \end{bmatrix} \tag{5}$$

is set up where $\sigma_{s,j} = 1.0\ mm + s_j \cdot 0.02\ mm/m$, $\sigma_\beta = 2.5\ mgon$ and $\sigma_t = 2.5\ mgon$ are chosen corresponding to the manufacturer's specifications of the Leica Scan Station P20 [21]. As usual, the observations have to be assumed to be uncorrelated and Gaußian distributed because of the lack of correlation information.

This adjustment typically leads to the Gauß-Helmert model (GHM) – also known as general case of adjustment [29] – considering the used functional model. Thus, the residuals $\hat{\mathbf{v}}$ representing the deviations between observations $\mathbf{l}$ and approximated observations $\hat{\mathbf{l}}$ are minimized following the theoretical target function $\mathbf{v}^T\boldsymbol{\Sigma}_{ll}^{-1}\mathbf{v}$ [29, 44].

The strict solution of the GHM is explained in many publications [14, 22, 29, 30] so that a recapitulation is omitted here. For numerical reasons due to the large number of observations when approximating laser scans, the GHM is transformed to a Gauß-Markov model (GMM) [44]. This transformation is valid when working with TLS measurements [10].

The results of the approximation are the estimated parameters $\hat{\mathbf{p}}$ including their covariance matrix $\boldsymbol{\Sigma}_{\hat{p}\hat{p}}$. Here, – as already stated – the estimated focal length is the most meaningful parameter for the present application. Furthermore, the post-fit residuals $\hat{\mathbf{w}}$ of each sampling point, also called discrepancies in a GHM [15], are estimated. They can be used to analyze local systematic deformations of the telescope's surface. For an intuitive analysis of these deformations, the residuals' sign is defined here as follows: negative residuals are under/outside the reflector, positive residuals are above/inside the reflector.

4 Preprocessing of the point cloud

Principially, the deformation analysis could be performed already based upon the original measurements and the adjustment of the parameters including the focal length and the post-fit residuals at different elevation angles of the telescope. However, this would – at this point – produce misleading results suffering from missing preprocessing steps. These steps of data reduction, object segmentation and TLS self-calibration are presented here.

4.1 Data reduction

Data reduction might be a usual step in TLS point cloud preprocessing. Usually, the aim is to improve the manageability of the data memory and processing time by reducing the data volume when the object was over-sampled initially [19, 20, 45]. Only in the recent past, data reduction has been analyzed regarding its potential for rigorously achieving unbiased results in area-based surface analysis [10, 14].

In fact, estimates of surfaces from a TLS point cloud can be biased if the surface suffers from an incomplete representation. Additionally, this bias varies when changing the scanning geometry. This is always the case if unknown, non-parameterized deformations exist on the surface since these deformations result in systematic errors.

The reason can be found in the sampling of surfaces when using a TLS. Due to the sampling by constant angular increments, the sampling density on the surface is irregular in nearly all cases. Thus, areas that are more densely sampled have a higher impact on the parameter estimation than sparsely sampled areas. If deformations exist which bias the parameter estimation, their influence depends on the ratio of points covering these deformations and those which are unaffected. Hence, by reducing the number of data to gain similar point distances, this effect of varying bias due to an irregular point sampling reduces.

This has been shown theoretically by [10] and it can be confirmed by the present study when analyzing the measurements of the year 2010 [31]. For approximating the whole point cloud of about 350 million points, the adjustment had to be implemented in C++ on a high-performance processor using parallel computing. The sampling density of this point cloud can be studied in Figs. 3 (top) and 4 (left): near the main reflector's vertex, the sampling points are close together. Their spacing increases to the borders of the reflector.

In a parallel processing chain, the data has been reduced to a nearly constant grid leading to a nearly homogeneous and constant sampling density of 1 million points (Figure 4, right). The least-squares adjustment for this data set was implemented in Matlab on a common processor. Figure 5 shows the differences of the estimated focal lengths between complete data and the reduced one.

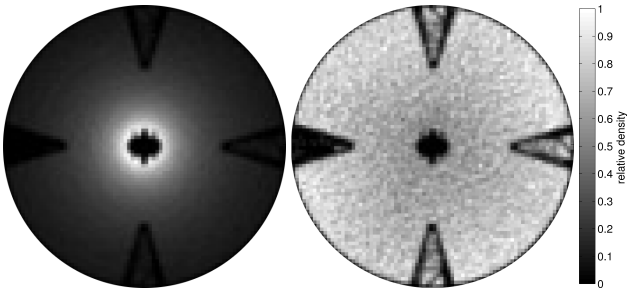

Fig. 4. Relative sampling densities of scans when comparing the complete point cloud (left) and the reduced one (right), shown from top-view of the main reflector [31].

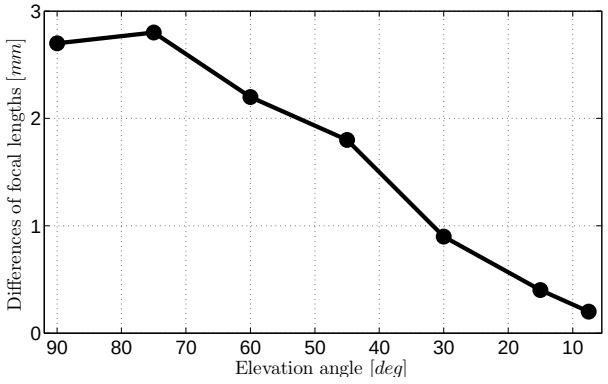

Fig. 5. Differences between the focal length estimations when using the original, unreduced point cloud and when using the reduced point cloud; used data from the year 2010.

Clearly, there is a bias between both estimates that decreases proportionally to the elevation angle of the telescope. This bias can be traced back to local deformations on the main reflector due to two reasons: (1) the magnitude of the local deformations decreases with decreasing elevation angle (see also the post-fit residuals in Figure 11). (2) The local deformations are located near the main reflector's vertex – at the densest sampling regarding the non-reduced point cloud. Thus, these deformations impact the parameter estimation by a larger magnitude when approximating the non-reduced point cloud compared to when approximating the reduced one.

Consequently, due to unknown and non-paramterized local deformations of the surface, the parameter estimation would be variably biased when using the complete point cloud with irregular point sampling. Data reduction reduces this impact – robust estimation as also suggested in [10] would not be a better solution: since several areas of local deformations exist, they cannot all be separated from the undeformed parts.

Fig. 6. Detailed picture of the reflector surface showing single panels and its perforated outer ring.

4.2 Object segmentation

Generally, object segmentation describes the separation of the object of interest from the surrounding background not being of interest. Therefore, the method of separation is application-specific in most cases. This can range from semantic segmentation [33] to geometric segmentation [43] for, e.g., plant analysis. In the present case, the object segmentation directly evolves from the construction of the main reflector: (1) its partial transparency and (2) its subdivision into single panels. Both circumstances can be seen in Figure 6.

(1) The outer ring of the telescope of 10 m width is perforated to reduce aerodynamic resistance. Scanning perforated surfaces likely leads to data artefacts, mixed pixels or other systematic deviations [39]. Thus, these parts are not suited for TLS measurements what could also be seen when studying the radiometric data measured by the scanner. Additionally, first investigations also show that the outer ring seems to be deformed compared to the rest of the main reflector. Consequently, these parts are eliminated from the point cloud so that the remaining main reflector being analyzed is 80 m in diameter.

(2) The main reflector does not equal a solid entity but consists of 2360 panels including the perforated outer ring with 1496 solid panels [28]. The distance between neighboring panels ranges from several millimeters to a few centimeters – in any case big enough for a laser spot to fit in the gap with foot prints of about 10 mm at distances of 30 – 40 m [21].

Thus, only points are considered further that are located without any doubt on a panel surface. This is guar-

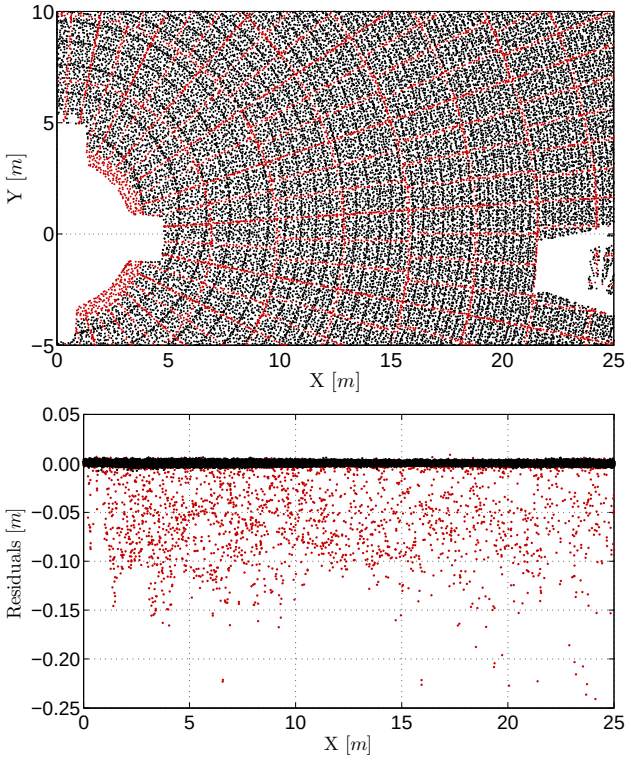

Fig. 7. Detailed view of a section of the point cloud indicating points that are segmented as corresponding to the main reflector (black) and points that are eliminated (red) due to their position between panels (top); corresponding post-fit residuals of the same segment (bottom).

anteed by omitting all points between the panels as well as the ones with a distance less than a few centimeters to the panels' borders. For this purpose, all panels are mapped using the radiometric measurements of the TLS. This is possible since the reflectivity of the signal is high only on the panels themselves and not inbetween.

Figure 7 indicates the benefit: it displays the segmentation of the paraboloid and the omitted points for a part of the main reflector (top). Furthermore, the post-fit residuals corresponding to the same part are shown (bottom). Clearly, the post-fit residuals of the points lying on the panels are in the range of only a few millimeters. On the contrary, the ones corresponding to the omitted points are all of significantly larger magnitude and also all negative – thus, their measured distance is too long. Hence, not eliminating these points would significantly degrade the parameter estimation and deformation analysis.

From view of the VLBI, these two types of data segmentation are also constructive: signal rays, which do not hit the main reflecting surface but perforation holes or panel gaps are not reflected to the subreflector in the right angle and will be directed into the receiver feed horn only by accident and to a negligible amount. Furthermore, since the outer panels are deformed to a larger extent, their reflections into the feed horn are minimized as well. For this reason, both steps of the data segmentation process exactly match the consequences for the VLBI observations.

4.3 Laser scanner self-calibration

Laser scanner calibration has become a wide field of research since TLS are used more and more for analyses where highest accuracy is of interest [6, 42]. Without calibration, the systematic errors following from unavoidable misconstruction of the TLS can easily outnumber the random errors so that the interpretation of deformations can be totally misleading [13]. This can be seen for the present application in Figure 8 where the post-fit residuals of either the uncalibrated TLS measurements (top) and the calibrated ones (bottom) are shown. The used calibration strategy will be introduced in the following.

Existing strategies for self-calibrating laser scanners are all based on using a calibration field consisting of several targets or planes scanned from different stations. By parameterizing these substitute objects, the parameter deviations that are revealed by spatial coordinate transformations can directly be related to the TLS specific systematic errors [2, 3, 7, 8, 23, 27, 32]. Crucial are an appropriate laser scanner construction model for parameterizing the calibration parameters and a calibration field enabling an accurate and reliable parameter estimation [24–26].

In [13], a new strategy for self-calibration of a TLS is proposed. It considers scanning one single object uniquely where the deviations to an approximated surface are directly used for estimating the calibration parameters. This object should be very large since it needs to cover nearly the whole panoramic scan. Thus, the calibration field simply consists of one single object sampled by a very large number of points.

This calibration has been evaluated using the present application of approximating the Effelsberg radio telescope [13]. As a result, the calibrated TLS observations are free of systematic errors. Therefore, the following calibration parameters that are mostly also used in [37, 38] are considered:

- c: horizontal collimation error, i.e., non-orthogonality between collimation axis and trunnion axis
- i: trunnion axis error, i.e., non-orthogonality between trunnion axis and vertical axis
- h: vertical index error (vertical collimation error), i.e., deviation of vertical angle from zero at zenit

- $\varepsilon_{t,1}, \varepsilon_{t,2}$: eccentricities of horizontal graduated circle, i.e., deviation between geometrical mean of horizontal graduated circle and vertical axis
- $\varepsilon_{\beta,1}$: eccentricity of vertical graduated circle, i.e., deviation between geometrical mean of vertical graduated circle and trunnion axis
- e_z: vertical eccentricity of collimation axis, i.e., vertical distance between collimation axis and trunnion axis

These parameters are integrated in the adjustment by expanding the functional model by

$$\tilde{\beta}_j = \pm \arccos\left(\cos i \cdot \cos c \cdot \cos \beta_j - \sin i \cdot \sin c\right) + h + \varepsilon_{\beta,1} \cdot \cos \beta_j + \arcsin \frac{e_z}{s_j} \tag{6}$$

$$\tilde{t}_j = t_j + \arctan\left(\frac{\cos i \cdot \tan c}{\sin \beta_j} + \frac{\sin i}{\tan \beta_j}\right) + \varepsilon_{t,1} \cdot \sin t_j + \varepsilon_{t,2} \cdot \cos t_j \tag{7}$$

so that $\tilde{\beta}_j$ and $\tilde{t}_j$ – representing the angles free of systematic errors – are integrated in eq. (4) instead of solely β_j and t_j. Consequently, the vector of parameters $\mathbf{p}$ parameterizing the main reflector needs to be enlarged by the calibration parameters

$$\mathbf{p} = \left[X_v, Y_v, Z_v, \varphi_x, \varphi_y, f, c, i, h, \varepsilon_{t,1}, \varepsilon_{t,2}, \varepsilon_{\beta,1}, e_z\right]^T. \tag{8}$$

Further parameters, e.g., a zero error of the distance unit, are not predictable based on the given network configuration [13]. Thus, this calibration model only considers systematic errors due to the beam divergence.

These calibration parameters are estimated at each elevation angle separately. Otherwise, the results would not be free of systematic errors. This leads to calibration parameters for the Leica Scan Station P20 that are not constant and, thus, not physically interpretable. The parameters themselves are not of interest here but the results show that after calibration, the systematic errors are indeed eliminated. A deeper explanation and evaluation of this dynamic calibration is given in [13].

Figure 8 shows the results of the approximation before (top) and after calibration (bottom) of the point cloud at an elevation angle of 75 *deg*. Clearly, the systematic deviations that are symmetric to the TLS x- and y-axis are eliminated. The remaining effects on the surface are interpreted together with the results corresponding to the other elevation angles at the end of this study. At this point, an evaluation of the calibration regarding the noise reduction will also be given.

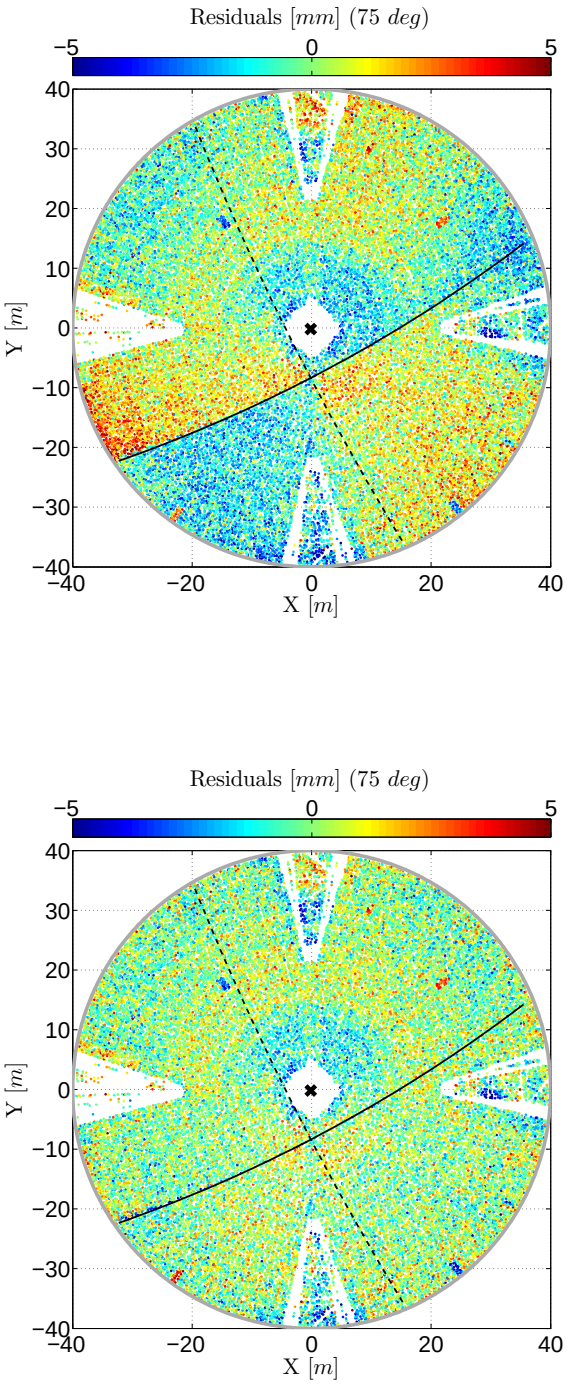

Fig. 8. Post-fit residuals of the approximation at an elevation angle of 75 *deg* shown in object coordinate system $[X, Y, Z]$; TLS x-axis, (lined), y-axis (dashed) and station (cross); before calibration (top) and after calibration (bottom).

5 Final deformation analysis

After performing the three steps of preprocessing, the final results can be analyzed for deformations. As already stated in the previous sections, the effects of interest are: the focal length variation – indicating the global deformation – and the post-fit residuals of the adjustment – indicating local deformations and the TLS precision. Both types of deformations are analyzed in the following. Supplemental results of the parameter estimation are afterwards also shortly examined.

5.1 Focal length variations: global deformation

The varying focal lengths are depicted in Figure 9 and in Table 1. Figure 9 displays the final results together with the results that would occur without calibrating the TLS. Furthermore, the results of the measurements performed in 2010 are shown.

The benefit of calibrating the TLS is clearly visible. The extreme variations of the focal length vanish after calibration – their prior opposite peaks resulted from the scanning process itself: the TLS horizontally rotates 180 deg for each scan. Thus, its systematic errors act oppositionally in consecutive elevation angles leading to the calibrated estimates being much smoother and more plausible. This effect is only small at high elevation angles since the systematic errors impact the estimation rather symmetrically at these geometries (see also Figure 3) so that the effects are balanced.

Comparing the results to the focal length estimates of the measurements performed in the year 2010 [11, 15, 31], significant differences occur: the variation of the focal length is smaller and it follows a linear trend instead of the quadratic one of the improved estimation. However, with a better measurement setup and improved analysis tools, we were able to detect the deficits of the 2010 project: (1) a Leica HDS 6100 TLS had been used leading to significantly noisier measurements. (2) The TLS had been mounted rigidly to the subreflector. Thus, the complete TLS had rotated vertically so that gravitational forces acted on its servomotors actuating the rotation around the scanner's vertical axis. Since these gravitational forces do not act in the direction of the scanners' vertical axis due to its vertical rotation, they are not considered by the manufacturers during construction. Hence, they may have produced further systematic effects leading to systematic measurement errors. This situation can also be seen at the focal length estimation of 7.5 deg showing inexplicable deviations.

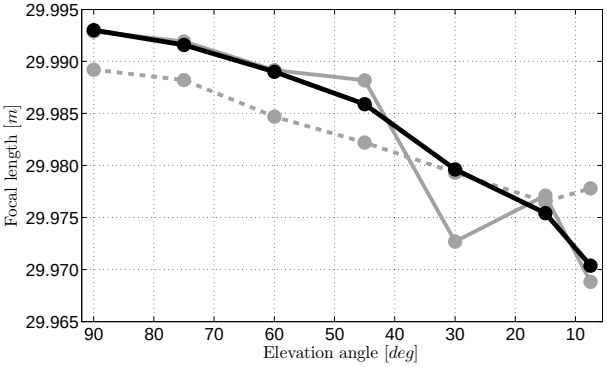

Fig. 9. Estimated focal lengths based on the preprocessed point clouds of the measurements performed in the year 2010 (gray dashed) and in the year 2013 with uncalibrated TLS (gray lined) and dynamically calibrated TLS (black, final estimate of the focal length).

Thus, the new results are considered to be more reliable. Here, the focal length $\hat{f}$ decreases quadratically by 22.7 mm when tilting the radio telescope from 90 deg elevation angle to 7.5 deg. The corresponding standard deviations $\hat{\sigma}_f$ are in the range of 0.03 – 0.09 mm (Table 1). However, this magnitude is too optimistic due to the neglection of correlations in the stochastic model (eq. 5). For a realistic magnitude, the number of effective measurements considering correlations would have to be estimated [18]. This number would be significantly smaller than the number of actual observations similar to the situation at, e.g., GPS observations [17].

5.2 Post-fit residuals: local deformations and TLS precision

The post-fit residuals $\hat{\mathbf{w}}$ consist of two parts: the first one describes the random errors resulting from the precision of the measurements, i.e., the random TLS errors with zero mean. The second part describes true local deformations of the main reflector, indicated by a regional shift from zero mean. The respective paraboloid zones could have already been guessed from Figure 8 (bottom) where some parts seem to deviate from zero significantly. A third part, i.e., remaining systematic errors of the TLS, is not assumed to be integrated in the post-fit residuals due to the calibration.

Table 1. Estimated focal lengths $\hat{f}$, the corresponding standard deviations $\hat{o}_f$ and the resulting focal length variations $\Delta\hat{f}$.

value	*90 deg*	*75 deg*	*60 deg*	*45 deg*	*30 deg*	*15 deg*	*7.5 deg*
$\hat{f}\ [m]$	29.9930	29.9916	29.9890	29.9859	29.9796	29.9754	29.9704
$\hat{o}_f\ [mm]$	0.03	0.04	0.06	0.06	0.09	0.06	0.08
$\Delta\hat{f}[mm]$	-	-1.4	-4.0	-7.1	-13.4	-17.6	-22.7

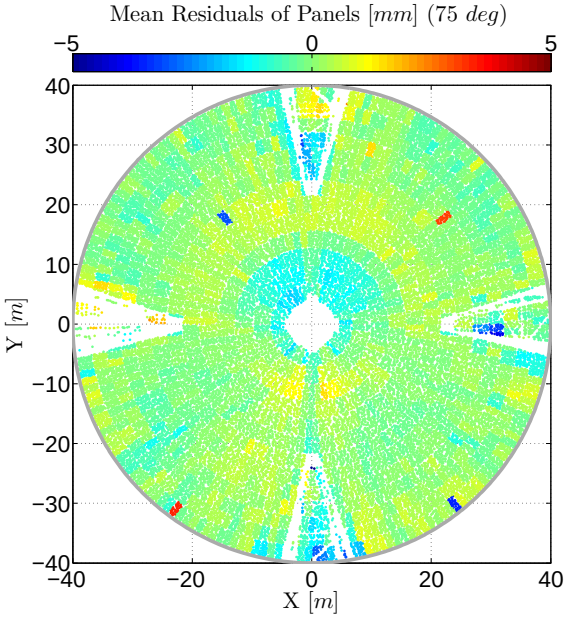

Fig. 10. Mean post-fit residuals of each panel after dynamic calibration of 75 *deg* elevation angle shown in object coordinate system $[X, Y, Z]$ where the X-axis equals the tilting axis of the telescope; negative residuals are under/outside the reflector, positive residuals are above/inside the main reflector.

5.2.1 Local deformations

For analyzing the local deformations, a deeper knowledge of the main reflector's construction is helpful: since the position of each panel and also the sampling points for each panel are known, the mean post-fit residual of each panel can be calculated. This averaging of all residuals of each individual panel produces the mean shift of each panel. The random errors are filtered out.

Figure 10 shows the results of this procedure for the 75 *deg* elevation angle. The benefit of averaging each panel for interpretation is directly visible. Here, individual panels are discernable because all sampling points of a panel are illustrated in the color of its mean residual value. Six panels significantly deviate by approx. 5 *mm* from the best-fit paraboloid surface. Four of them had been misaligned on purpose for the control of a holography. The two behind the right-hand quadruped leg are obviously also misaligned – but unintendedly. All other panels deviate by less than ± 2 *mm*. This statement also holds for the other six elevation angles; their results are shown in Figure 11.

Analyzing the residuals of less than ± 2 *mm*, superposed area-based systematics seem to evolve: at the elevation angles of 90 – 60 *deg*, deformed parts exist directly over and under the reflector's vertex. They decrease proportionally to the elevation angle. Furthermore, from directly under the vertex in down direction, we can identify panels with constant negative deviations throughout all elevation angles. As already stated in Section 4.1 (Data Reduction), all of these deviations necessitate the data reduction.

Since all of these effects are symmetric to the tilting axis of the radio telescope defined as the X-axis in Figure 11, they can be assumed to represent true local deformations that are due to gravity. In general, it can be stated that the area-based deformations appear to be smallest for the 30 *deg* and 45 *deg* elevation angles. This matches quite well the background information that the telescope surface was adjusted following holography measurements at 32 *deg* elevation [16].

5.2.2 TLS precision of distance measurements

The TLS precision can be assessed when calculating the standard deviation $\hat{o}_w$ of the post-fit residuals. As these post-fit residuals approximately point into line-of-sight of the TLS, the precision mainly depends on the quality of the distance measurements. This transfer is valid since the construction of the panels can be assumed to be more precise than the measurements: the accuracy of an individual panel is claimed to be 0.3 – 0.5 *mm* [28].

These standard deviations are listed in Table 2 for the approximations before and after calibration. The ones before calibration are just given for evaluating the improvement of the adjustment by calibration. They range from 1.5 – 2.1 *mm*. The standard deviation after calibration is 1.3 *mm* with no significant variations over the full range of elevations angles. The results at 90 *deg* and 75 *deg* elevation angle are slightly worse due to the surface deformations revealed before.

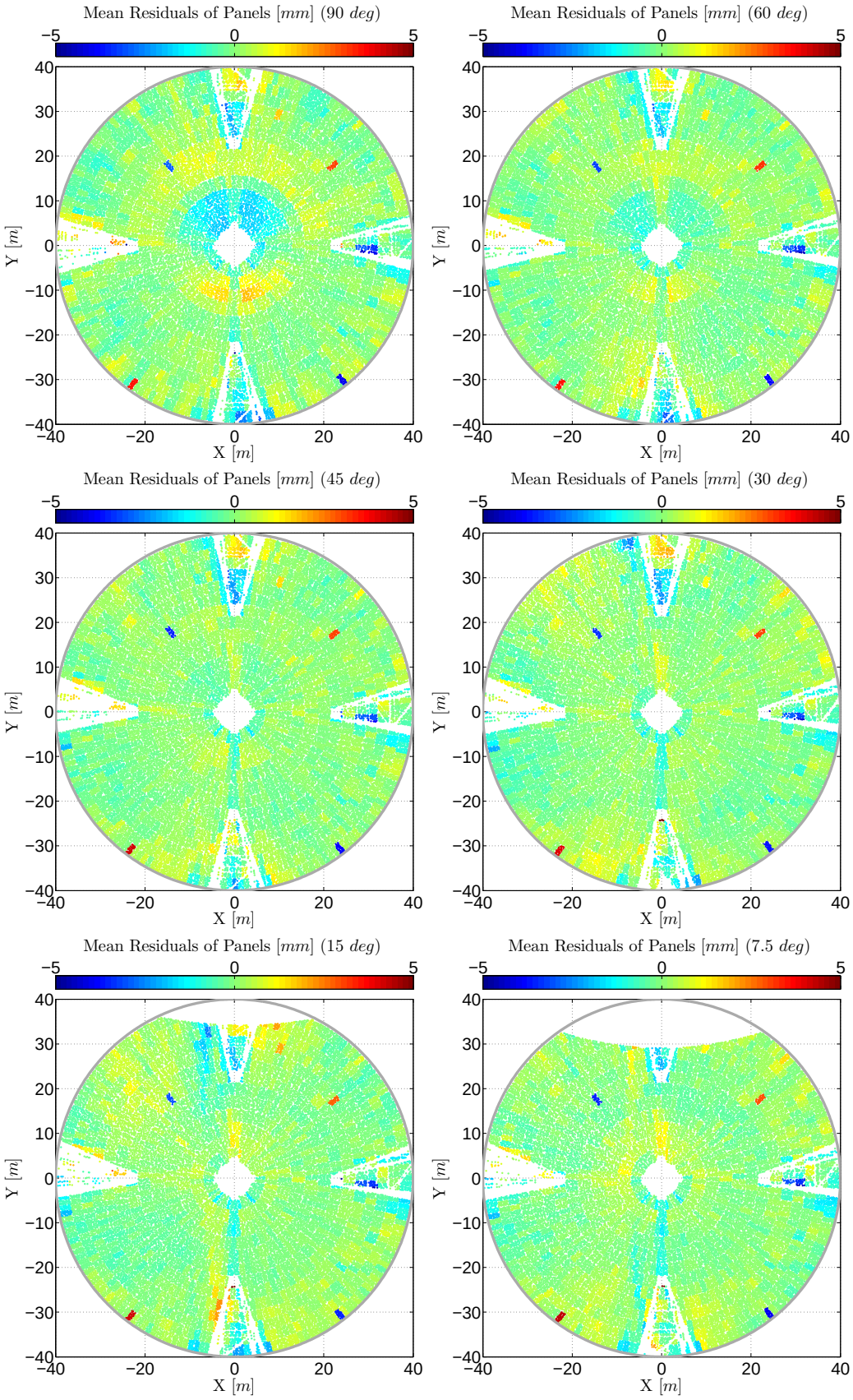

Fig. 11. Mean post-fit residuals of each panel after dynamic calibration of all seven elevation angles shown in object coordinate system $[X, Y, Z]$ where the X-axis equals the tilting axis of the telescope; negative residuals are under/outside the reflector, positive residuals are above/inside the main reflector.

Table 2. Estimated standard deviation $\hat{\sigma}_w$ of the post-fit residuals $\hat{\mathbf{w}}$ before and after calibration of the measurements.

value	*90 deg*	*75 deg*	*60 deg*	*45 deg*	*30 deg*	*15 deg*	*7.5 deg*
$\hat{\sigma}_w$ $[mm]$ (prior calibration)	1.45	1.60	1.56	1.47	2.05	1.88	1.83
$\hat{\sigma}_w$ $[mm]$ (dynamic calibration)	1.35	1.32	1.28	1.27	1.29	1.31	1.30

The standard deviation of $1.3\ mm$ can be regarded as the true level of noise of the distance measurements of the Leica Scan Station P20. This magnitude is comparable to the accuracy of $\sigma_s = 1.6 - 1.8\ mm$ at distances of $s = 30 - 40\ m$ assumed in the stochastic model (eq. 5). This is also an indicator for the consistency of the approximation.

5.3 Supplemental results of the parameter estimation

Besides the focal length variations and the post-fit residuals, the parameter estimation yields to several other results. These concern the estimates of the five transformation parameters $[X_v, Y_v, Z_v, \varphi_x, \varphi_y]^T$, the ones of the seven calibration parameters $\left[c, i, h, \varepsilon_{t,1}, \varepsilon_{t,2}, \varepsilon_{\beta,1}, e_z\right]^T$ as well as the correlations between the parameters. All aspects are briefly addressed here.

The transformation parameters indicating the spatial transformation between TLS station and main reflector follow a systematic trend between the different elevation angles of the telescope. Since the TLS is not levelled and there is no absolute external link between both coordinate systems, these transformations are only relative and do not represent the absolute movement of the telescope. The geodetic datum is not fixed between the different elevation angles.

The estimates of the calibration parameters are not discussed here. In [13], a detailed derivation of the here used dynamic calibration is given. There, the combination of the used calibration parameters and their estimates are investigated in view of stability, correlation and the general network configuration.

Between several parameters, non-negligible correlations exist. Their magnitude depends on the elevation angle of the telescope in most cases. This statement holds for the correlations within the three groups of parameters (form, transformation and calibration parameters) as well as between them. For deeper statements, see [13].

6 Conclusion and outlook

The present study yields an improved deformation analysis of the main reflector of the Effelsberg radio telescope. The processing rests upon integrating model knowledge into the analysis by parameterizing the main reflector as a rotational paraboloid. This enables detecting a global deformation of the main reflector by a decrease of its focal length of $22.7\ mm$. Additionally, local deformations are revealed on its surface by misaligned surface panels and sections of systematic deviations. Both results will help to significantly improve the baseline estimation in VLBI where the signal path of the received signal directly depends on the focal length and the surface precision of the main reflector.

Apart from these application-specific results, the strategy for deformation analysis is explained in detail focused on an improved measurement concept and three steps of preprocessing including data reduction, object segmentation and TLS self-calibration. It is highlighted that without the implementation of these steps, the deformation analysis could not have been performed reliably – and especially not with this significance. While the step of object segmentation seems to be trivial, the need for an appropriate data reduction and TLS calibration has not been considered in the literature until recently.

Thus, the improved deformation analysis presented here can be regarded as a result of steady enhancement of applying laser scanner measurements to surface analysis. Transferring the proposed steps of measurement and data processing to other applications and studies would, hence, benefit the general ability of using laser scanner measurements for area-based deformation analyses or general surface investigations where high accuracy is of interest.

References

[1] Artz T., Springer A. and Nothnagel A., A complete VLBI delay model for deforming radio telescopes: the Effelsberg case, *J. Geod.* 88 (2014), 1145-1161.

[2] Chow J. C. K., Lichti D. D. and Glennie C., Point-based versus plane-based self-calibration of static terrestrial laser scanners,

Int. Arch. Photogramm. Remote Sens. Spat. Inf. Sci. 38 (2011), 121-126.

[3] Chow J. C. K., Lichti D. D., Glennie C.and Hartzell P., Improvements to and comparison of static terrestrial lidar selfcalibrationa methods, *Sensors* 13 (2013), 7224–7249.

[4] Clark T. A. and Thomsen P., *Deformations in VLBI antennas*, Nasa Technical Memorandum 100696, NASA, Greenbelt, Md., Report, 1988.

[5] Dutescu E., Heunecke O. and Krack K., Formbestimmung bei Radioteleskopen mittels Terrestrischem Laserscanning, *Allgem. Verm. Nachr.* 6 (2009), 239–245.

[6] Eling D., *Terrestrisches Laserscanning für die Bauwerksüberwachung*, Ph.D. thesis, Wissenschaftliche Arbeiten der Fachrichtung Geodäsie und Geoinformatik der Leibniz Universität Hannover, no. 282, 2009.

[7] Gielsdorf F., Rietdorf A. and Gründig L., A concept for the calibration of terrestrial laser scanners, in: *FIG Working Week 2004, Athens, Greece, May 22-27, 2004*, 2004.

[8] Gordon B., *Zur Bestimmung von Messunsicherheiten terrestrischer Laserscanner*, Ph.D. thesis, Fachbereich Bauingenieurwesen und Geodäsie der Technischen Universität Darmstadt, D 17, 2008.

[9] Hachenberg O., *Studien zur Konstruktion des 100-m-Teleskops, Beiträge zur Radioastronomie*, Max-Planck-Institut für Radioastronomie Bonn, 1, Dümmler, Bonn, 1968.

[10] Holst C., Artz T. and Kuhlmann H., Biased and unbiased estimates based on laser scans of surfaces with unknown deformations, *J. Appl. Geodesy* 8 (2014), 169–184.

[11] Holst C., Dupuis J., Paulus S. and Kuhlmann H., Flächenhafte Deformationsanalysen mit terrestrischen und Nahbereichslaserscannern - eine Gegenüberstellung anhand von Beispielen, *Allgem. Verm. Nachr.* 7 (2014).

[12] Holst C. and Kuhlmann H., Bestimmung der elevationsabhängigen Deformation des Hauptreflektors des 100m- Radioteleskops Effelsberg mit Hilfe von Laserscannermessungen, in: *Schriftenreihe DVW, Band 66: Terrestrisches Laserscanning - TLS 2011 mit TLS-Challenge, Wißner*, pp. 161–180, Augsburg, 2011.

[13] Holst C. and Kuhlmann H., Aiming at self-calibration of terrestrial laser scanners using only one single object and one single scan, *J. Appl. Geodesy* (2014), submitted.

[14] Holst C. and Kuhlmann H., *Impact of spatial point distributions at laser scanning on the approximation of deformed surfaces*, Ingenieurvermessung 14. Beiträge zum 17. Internationalen Ingenieurvermessungskurs, A. Wieser, Zurich, 2014, pp. 269–282.

[15] Holst C., Zeimetz P., Nothnagel A., Schauerte W. and Kuhlmann H., Estimation of focal length variations of a 100-m radio telescope's main reflector by laser scanner measurements, *J. Surv. Eng.* 138 (2012), 126–135.

[16] Kraus A., personal communication, Max Planck Institute for Radio Astronomy, July 2014.

[17] Kuhlmann H., Importance of Autocorrelation for Parameter Estimation in Regression Models, in: *Proceedings 10th FIG International Symposium on Deformation Measurements*, pp. 354–361, 2001.

[18] Kuhlmann H., Kalman-filtering with coloured measurement noise for deformation analysis, in: *Proceedings, 11th FIG Symposium on Deformation Measurements*, Santorini, Greece, 2003.

[19] Lee K. H., Woo H. and Suk T., Data reduction methods for reverse engineering, *Int. J. Adv. Manuf. Technol.* 17 (2001), 735–743.

[20] Lee K. H., Woo H. and Suk T., Point data reduction using 3D grids, *Int. J. Adv. Manuf. Technol.* 18 (2001), 201–210.

[21] Leica Geosystems, Leica ScanStation P20, industry's best performing ultra-high speed scanner, www.leica-geosystems.de, 30.07.2014.

[22] Lenzmann L. and Lenzmann E., Strenge Auswertung des nichtlinearen Gauß-Helmert-Modells, *Allgem. Verm. Nachr.* 2 (2003), 68–73.

[23] Lichti D. D., Error modelling, calibration and analysis of an AMCW terrestrial laser scanner system, *ISPRS J. Photogramm.* 61 (2007), 307–324.

[24] Lichti D. D., The impact of angle parameterisation on terrestrial laser scanner self-calibration, *Int. Arch. Photogramm. Remote Sens. Spat. Inf. Sci.* 38 (2009), 171–176.

[25] Lichti D. D., Terrestrial laser scanner self-calibration: Correlation sources and their mitigation, *ISPRS J. Photogramm.* 65 (2010), 93–102.

[26] Lichti D. D., Chow J. and Lahamy H., Parameter de-correlation and model-identifcation in hybrid-style terrestrial laser scanner self-calibration, *ISPRS J. Photogramm.* 66 (2011), 317–326.

[27] Lichti D. D., Gordon S. J. and Tipdecho T., Error models and propagation in directly georeferenced terrestrial laser scanner networks, *J. Surv. Eng.* 131 (2005), 135–142.

[28] Max Planck Institute for Radio Astronomy, *Technical data of the 100m-telescope*, http://www.mpifrbonn.mpg.de/245888/specs, August 2014.

[29] Mikhail E. M. and Ackermann F., *Observations and least squares*, Dun-Donelly, New York, 1976.

[30] Neitzel F., Generalization of total least-squares on example of unweighted and weighted 2D similarity transformation, *J. Geod.* 84 (2010), 751–762.

[31] Nothnagel A., Eichborn M. and Holst C., Improved focal length results of the Effelsberg 100 m radio telescope, in: *21st Meeting of the European VLBI Group for Geodesy and Astronomy* (N. Zubko and M. Poutanen, eds.), pp. 55–60, Reports of the Finnish Geodetic Institute, Espoo, Finland, March 5-8 2013.

[32] Rietdorf A., *Automatisierte Auswertung und Kalibrierung von scannenden Messsystemen mit tachymetrischem Messprinzip*, Ph.D. thesis, DGK, C 582, 2005.

[33] Roscher R., *Sequential learning using Incremental Import Vector Machines for semantic segmentation*, Ph.D. thesis, DGK, C 716, 2013.

[34] Sarti P., Abbondanza C., Petrov L. and Negusini M., Height bias and scale effect induced by antenna gravitational deformations in geodetic VLBI analysis, *J Geod* 85 (2011), 1–8.

[35] Sarti P., Abbondanza C. and Vittuari L., Gravity-dependent signal path variation in a large VLBI telescope modelled with a combination of surveying methods, *J Geod* 83 (2009), 1115–1126.

[36] Sarti P., Vittuari L. and Abbondanza C., Laser scanner and terrestrial surveying applied to gravitational deformation monitoring of large VLBI telescopes' primary reflector, *J Surv Eng* 135 (2009), 136–148.

[37] Schneider D. , Calibration of a Riegl LMS-Z420i based on a multi-station adjustment and a geometric model with additional parameters, *Int. Arch. Photogramm. Remote Sens. Spat. Inf* 38 (2009), 177–182.

[38] Schneider D. and Schwalbe E., Integrated processing of terrestrial laser scanner data and fisheye-camera image data, *Int. Arch. Photogramm. Remote Sens. Spat. Inf. Sci.* 37 (2008).

[39] Schulz T., *Calibration of a Terrestrial Laser Scanner for Engineering Geodesy*, Ph.D. thesis, ETH Zürich, 2007.

[40] Shankar N. U., Duraichelvan R., Ateequlla C. M., Nayak A., Krishnan A., Yogi M. K. S., Rao C. K., Vidyasagar K., Jain R., Mathur P., Govinda K. V., Rajeev R. B. and Danabalan T. L., Photogrammetric measurements of a 12-metre preloaded parabolic dish antenna, in: *Proceedings of the National Workshop on the Design of Antenna and Radar Systems (DARS), ISRO Telemetry Tracking and Command Network (ISTRAC)*, Bangalore, India, February 13-14 2009.

[41] Subrahmanyan R., Photogrammetric measurement of the gravity deformation in a cassegrain antenna, *IEEE T Antenn Propag* 53 (2005), 2590–2596.

[42] Wang J., *Towards deformation monitoring with terrestrial laser scanning based on external calibration and feature matching methods*, Ph.D. thesis, Wissenschaftliche Arbeiten der Fachrichtung Geodäsie und Geoinformatik der Leibniz Universität Hannover, no. 308, 2013.

[43] Weiss U. and Biber P., Plant detection and mapping for agricultural robots using a 3D lidar sensor, *Robot. Auton. Sys.* 5 (2011), 265–273.

[44] Wolf H., *Ausgleichungsrechnung. Formeln zur praktischen Anwendung*, Dümmler, Bonn, 1975.

[45] Zainuddin K., Setan H. and Majid Z., From laser point cloud to surface: data reduction procedure test, *Geoinformation Science Journal* 9 (2009), 1–9.